



Research papers

Neural network for the estimation of LFP battery SOH cycled at different power levels

C. Scarpelli^{a,*}, J. Gazzarri^b, T. Huria^c, G. Lutzemberger^a, M. Ceraolo^a^a Department of Energy, Systems, Territory and Constructions Engineering (DESTEC), University of Pisa, L. Lazzarino, 56122 Pisa, Italy^b MathWorks, Inc., Novi, MI 48377, USA^c Indian Railways, Mumbai 400020, India

ARTICLE INFO

Keywords:

Lithium battery
LFP
Aging
Feedforward network
State-of-life predictor

ABSTRACT

This work presents a method to quantify and estimate the degradation level of lithium-ion battery cell cycle aged at different power levels. Experimental results previously reported by the authors are analysed further, now with artificial intelligence workflows to establish a method to estimate the cells degradation rate, in term of State of Health. The neural network estimation capability is dependent on the type of input signal used for training, and the relative proportion of training vs. testing data. The development of a feedforward neural network which elaborates the information of voltage and current differences during sudden power changes significantly increased the predictive capability of the method, reaching State-of-Health estimation best-case errors lower than 1 %, in line with more complex Artificial Intelligence approaches found in literature. In addition, the results obtained with the feedforward neural network are then compared with a regression learning – based estimation function, trained and tested over the same dataset. As last test, both these two methods, trained with dataset coming from cycle aging experimental tests, are used to estimate the State of Health of a lithium cell aged due to calendar phenomena only.

1. Introduction

Degradation in resistance and capacity of lithium-ion battery (LIB) cells is an important factor determining the useful life of the battery for different applications. Since the creation of LiFePO_4 (LFP) lithium-ion cell [1], graphite/LFP cell batteries have grown in popularity in automotive and stationary power applications, since they provide high cycling capability, low cost, no reliance on cobalt or nickel, and resist fast-charging without compromising on safety. It is well known, however, that the faster the lithium-ion battery is charged or discharged, the faster its degradation proceeds. The decay in the life and performance of LIB due to fast charging is dependent upon the material of the battery components [2–5], layout of cells and modules in the battery pack, the charging protocol and the operating temperature. Out of these four, for any application, usually the battery (including the material of its anode and cathode and the layout of the individual cells in the battery pack) are determined by the manufacturer, while the battery charging protocol and operating temperature can be influenced by the user/end-consumer. Different users could charge the same battery in the same application differently in different ambient conditions hence this paper

studies the impact of these factors (controlled by the user) on the life and performance of an LIB.

Fast-charge aging comprises all aging processes that lead to a degradation of a battery cell when the battery cell is subjected to very high current levels [6–8]. Interfacial film formation, loss of contact between the electrode and the current collector and within the electrode itself, and structural degradation and dissolution of active materials are among the most frequently observed degradation phenomena in LIBs [9–11]. Globally, there is a rapid proliferation of fast charging as a mode of charging LIB powered vehicles through an ever-expansive network of charging stations and other power applications, to match the fueling time of conventional ICE powered vehicles. The increased use of fast charging is detrimental to the overall LIB life and its performance. It is therefore important to quantify the effects of fast charging on LIB's State-Of-Health (SOH) so as to identify the most critical factors affecting the battery, to enable consumers to take a prudent approach in adopting fast charging and for OEMs and battery engineers to design better energy management algorithms to improve battery life and performance. Aging of LIB is also strongly dependent upon its application and its handling by the user, depending upon the depth and rate of charge and discharge during its charge-discharge cycles [12]. In real-life applications, the LIBs

* Corresponding author.

E-mail address: claudio.scarpelli@phd.unipi.it (C. Scarpelli).<https://doi.org/10.1016/j.est.2023.107027>

Received 28 April 2022; Received in revised form 20 December 2022; Accepted 1 March 2023

Available online 29 April 2023

2352-152X/© 2023 Elsevier Ltd. All rights reserved.

Nomenclature

AI	Artificial Intelligence
BOL	Beginning-Of-Life
EKF	Extended Kalman Filter
EOL	End-Of-Life
FNN	Feedforward Neural Network
LFP	Lithium Iron Phosphate
LIB	Lithium-Ion Battery
LSTM	Long Short-Term Memory
RL	Regression Learning
RNN	Recursive Neural Network
SOC	State-Of-Charge
SOC _{EOD}	SOC reached at the End-Of-Discharge
SOH	State-Of-Health

do not operate on constant current-constant voltage cycles but are more variable. Often, the LIBs are subjected to extremely high current rates of charging or discharging, usually for time periods of around 15 min at a time during the lifetime of the battery by the user. For example, the LIB in the electric vehicle may be subjected to repeated fast charging or the stationary LIB storage provided in the EV fast charging station (to reduce the stresses on the grid during fast charging operations), would need to provide very high current peaks.

This paper demonstrates the application of AI functions to the study of cycling-induced battery cell degradation. To this end, LFP battery cycling data reported earlier [13] is now analysed by using machine learning functionalities today available in a commercial simulation software [14]. The experimental dataset was first used to train the AI functions and subsequently the remaining portion of the dataset was used to test the network to verify whether the predictions by the model agreed with the given experimental dataset. This training and testing was carried out in two different ways. In the first instance the dataset was randomised, and the net was trained on a random set of data extracted from the entire experimental database, in different percentage; then, it was subsequently tested on the remaining random data from the dataset. In the second scenario, the dataset was not randomised, therefore the estimation functions were trained on the dataset in chronological order, by using the data at the beginning of the dataset, and subsequently tested on the latter portion of the dataset.

This article is organized as follows: the authors first describe experimental procedure (Section 2); subsequently, the numerical approach is described with an outline of the main features of the function under consideration (Section 3). This section also presents a comparison among the AI-based cell degradation approaches considered here, and alternative methods from literature. Finally, the authors analyse and verify the method based on predictive accuracy evaluation also over an additional experimental test performed on a cell aged solely due to calendar phenomena (Section 4). Under this light it is possible to understand if the adopted estimation approaches trained with data coming from an aging cycle experimental test can be used also for cells aged in a different way.

2. Background and dataset

The experimental data used in this study was first published in [13], in which a cycle aging campaign was carried out on three nominally identical 60 Ah – 3.2 V LFP cells (whose main characteristics are summarised in Table 1). The experimental testing equipment was composed of a charging and discharging system driven by a Digatron® battery cell tester, and a thermostatic chamber. The battery tester is characterised by a voltage operating range up to 6 V and a maximum current up to 250 A. The thermostatic chamber operates in the range of 0 °C to 70 °C, with a

Table 1

Main cell characteristics.

Chemistry	Lithium-Iron-Phosphate (LFP)
Nominal capacity (Ah)	60
Voltage range (min/nominal/max) (V)	2.5/3.2/4
Maximum charge/discharge current (A)	180
Dimension (mm)	114 × 203 × 61
Weight (kg)	2.3

maximum set-point temperature oscillation equal to ± 0.5 °C. The cells under test were placed inside the thermostatic chamber and connected to the battery tester, which respectively measures the cell output voltage and current with an accuracy of 0.05 % and 0.1 % of full scale. The cell temperature is acquired by thermocouples placed in close contact of the surface of the cells themselves.

The three cells under analysis were subjected to aging cycles consisting of a fixed-duration constant power discharge, a consequent constant power charge, and a final fixed-duration rest phase, as shown in Fig. 1. The maximum constant power reached is called P_{cycle} . Every cell was tested with the same cycle test pattern except for the power level P_{cycle} : 250 W for cell A, 375 W for cell B and 500 W for cell C.

The cycles are continuously repeated until the cells under test have been fully aged. To determine the State-of-Health (SOH) based on the cell available capacity, the cycling is interrupted (e.g., every hundreds of cycles) to measure the cell capacity by integrating its extracted charge. This is done by performing a standard full charging/discharging test at reference conditions (specified by the manufacturer), after which the cell available capacity is defined as the cumulative charge extracted during the full discharging phase. This value is then used to calculate the cell SOH, expressed as the ratio between the current available cell capacity C_n and the cell capacity evaluated at the beginning of life (C_{BOL}), as shown in Eq. (1), where the subscript n stands for the n th cycle performed. In this way it is possible to correlate the cell SOH to the number of cycles performed.

$$SOH_n = \frac{C_n}{C_{BOL}} \quad (1)$$

In addition to SOH defined as shown above, we keep track of other aging specific parameters that provide further information on the degradation [13]. A significant parameter is the cell internal resistance coupled with the measurement of the cell temperature, which appeared to be well correlated to the cell SOH and has the advantage that we can

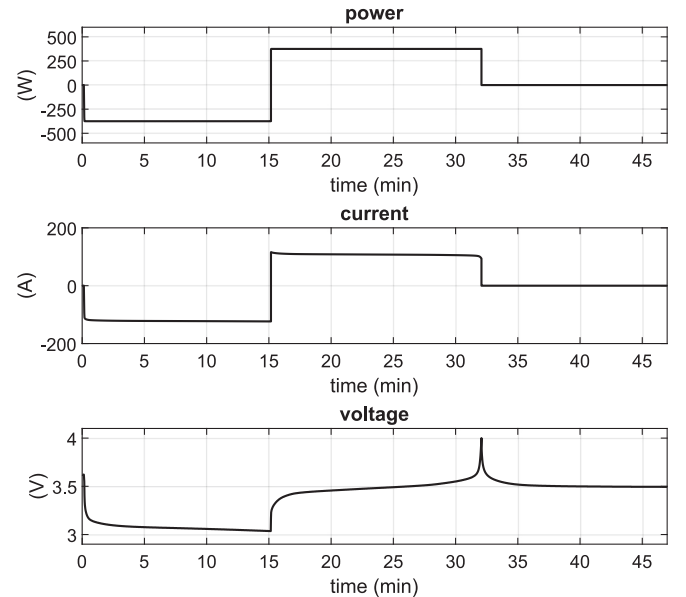


Fig. 1. Reference aging cycle pattern, cell B profiles shown.

measure it on-line, without the need to interrupt the cycling test.

The internal resistance R_i was calculated directly by the acquisition of the cell current and voltage data, measured during the cell cycling test. More specifically, it is the ratio between the voltage variation and the current variation in correspondence of the current step occurring as the discharge phase ends and the consequent charge phase begins. The Δt in Fig. 2 represents the time interval between the two adjacent samples of voltage and current used for the calculation of the cell internal resistance, which has always been set to 10 s in the experiments for this paper.

$$R_i = \frac{\Delta V}{\Delta I} \quad (2)$$

The lithium cell internal resistance is a function of many factors, the most significant of which are cell temperature, SOC, and SOH. Since the discharge time is always the same for all power levels tested, the SOC at which resistance is measured depends on power level because the internal resistance R_i was always evaluated at the End-Of-Discharge (EOD) phase. It must however be mentioned that different rising and falling edges may be considered, through the utilisation of much more sophisticated algorithms [15].

For the cell tested at low power (*cell A*, which cycles at 250 W) the SOC reached at the End-Of-Discharge (EOD), SOC_{EOD} , was around 70 % (named as “high SOC”), while *cell B* and *cell C* similarly reached a SOC_{EOD} respectively around to 50 % (middle SOC) and around 30 % (low SOC). All these results are summarised in Fig. 3, which, in the upper plots, shows the SOH trends for the three cells under analysis as a function of the number of cycles performed. Fig. 3 shows also internal resistance R_i , indicating cell temperature T_{cell} and three different SOC levels.

Fig. 3 clearly depicts the increase in degradation rate with increase in discharging power. In fact, results from our previous work indicate that discharging at twice the power output reduces the battery life by a factor of ten. It is therefore important to understand how internal resistance at a given cell temperature and SOC correlates with the cell SOH, and how this information could predict the future trend of the cell degradation itself. Main results are presented in the data set of Table 2.

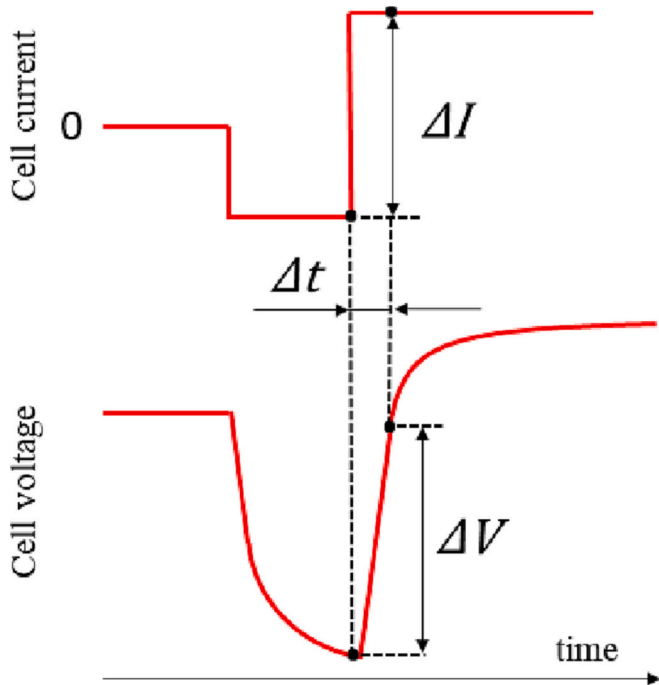


Fig. 2. Schematisation of current and voltage curves in correspondence of the change between discharge and charge phase.

The dataset is divided into three sections, based on the three cells analysed, which correspond to the three levels of cycling power tested (second column): low, middle, and high. Inside each section, for every cycle performed, information about the calculation of the cell internal resistance is displayed (columns ΔV , ΔI , and R_i itself), coupled with the measured cell temperature (column T_{cell}) and the respective cell SOH values (last column). In Table 2, few rows only for each section are shown: the very first cycle (Beginning of Life: BOL; first row of each section), one at intermediate level and the last one (End of Life: EOL; last row for each section). In this regard, the cell EOL level is defined as the moment in which the cell SOH reaches the threshold of 0.6. Based on this, a total of 4515 cycles are performed by *Cell A* cycling at 250 W, 958 cycles by *Cell B* cycling at 375 W and only 428 cycles are performed by the *Cell C* cycling at 500 W. The next chapters will illustrate how the dataset above described is elaborated by the neural net-based algorithms, in order to test the possibility to correctly predict the cell aging.

3. AI-based aging estimation

The difficulty in creating physical models based on first principles to describe the behaviour of a battery has led battery scientists to attempt to replace them with statistical methods that require training instead of parameterisation. If a function such as a neural network, capable of contemplating general nonlinearities of a system, is trained with experimentally measured data from a battery, the neural network will eventually act as a black box transfer function that mimics the behaviour of the battery whose data was used to train it. Potential advantages of this approach are accuracy, better response to corner cases, and computational efficiency. At the same time, they require vast amounts of data for training. This paper systematically investigates the influence of different predictors, training/testing data ratios, and randomisation on the accuracy of SOH estimation.

3.1. Feedforward Neural Network (FNN) approach

A feedforward neural network is a simple type of neural network in which the information flows in one direction, i.e., it does not have recurrency. Its simplicity makes it appealing for training since it is computationally inexpensive for hardware deployment because it consumes fewer resources than recurrent neural networks. It lacks, however, a notion of memory, so it requires moving averages as additional inputs if past information is needed.

In this section, the available dataset is used to train a feedforward neural network, created in MATLAB® using the function *feedforwardnet* [16]. First, the authors needed to determine which data to use as input. The base concept is to design a network capable of predicting the cell SOH by giving, as input information, some data that can be directly measured or calculated in the field. For this reason, observing the dataset of Table 2, possible input signals include P_{cycle} , SOC_{EOD} , ΔV , ΔI , R_i and T_{cell} .

All these vectors are normalised, linearly scaling them with respect to their respective maximum and minimum values among the entire dataset so that they are equally important to the AI function. To test the neural net behaviour as a function of the different information that could be given as inputs, different combinations of the columns above mentioned are tested as input variants, as shown in Table 3.

The output values do not need to be normalised since SOH is a normalised quantity, ranging from 1 (at Beginning-Of-Life “BOL”) to 0.6 (at End-Of-Life “EOL”). Fig. 4 illustrates the steps to follow to train the neural network.

The table on the left-hand side of Fig. 4 repeats the information from Table 2, showing predictors and responses in columns, and test cases in rows. The dataset is divided in *training* and *testing* subsets in which *training* refers to rows which include input and output data, to carry out the training of the neural network; on the other hand, *testing* refers to rows including only input data, while the outputs are estimated by the

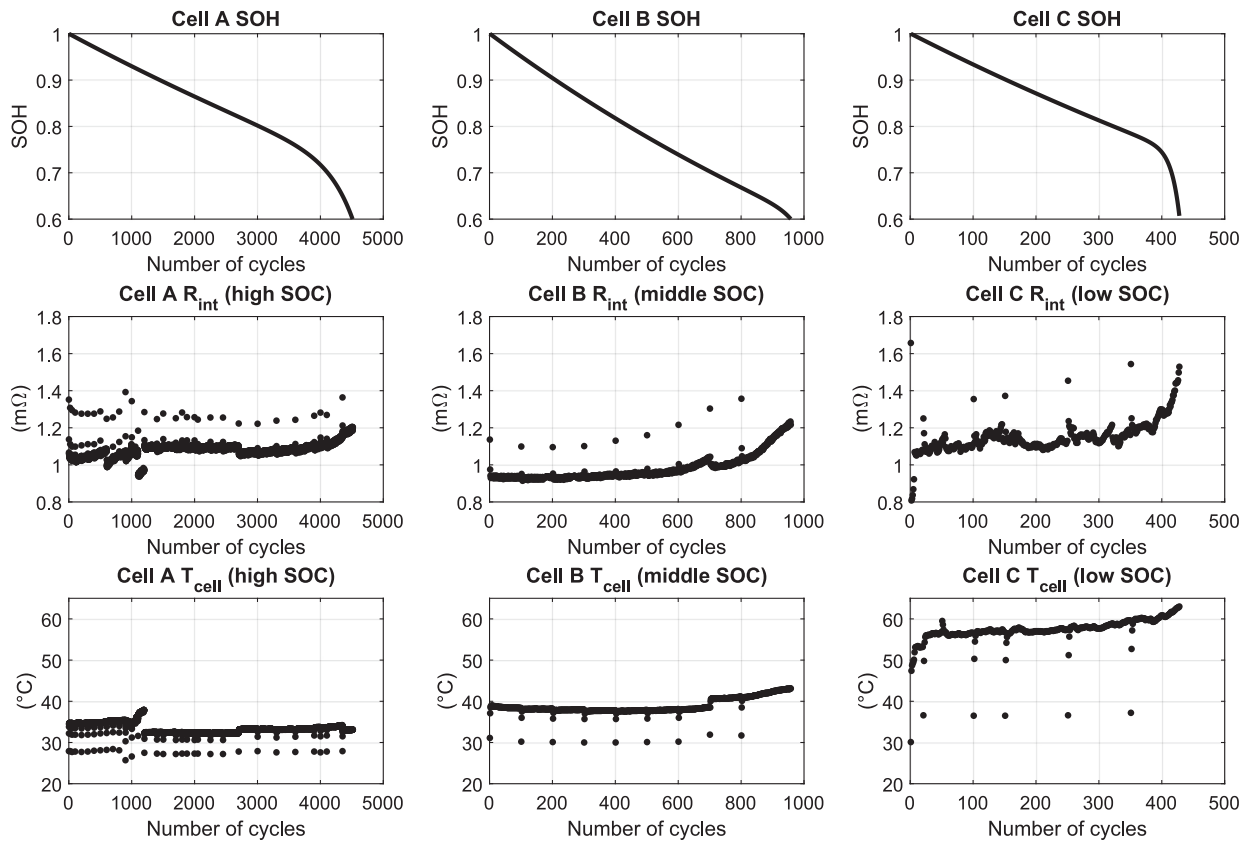


Fig. 3. Visualisation of the cell SOH in function of the number of cycles performed (upper plots) correlated with the calculated internal resistance coupled with the measured cell temperature (below plots).

Left side: cell A, middle: cell B, right side: cell C.

Table 2

Cycle aging information dataset.

Cell under test	Cycl. Pow. P_{cycle} (W)	EOD SOC SOC_{EOD} (%)	Number of cycles	ΔV (V)	ΔI (A)	R_i (mΩ)	T_{cell} (°C)	SOH
Cell A	250 (low)	70 (high)	1 (BOL)	0.209	154.59	1.352	27.9	1
		
			2000	0.168	154.56	1.087	31.7	0.86
Cell B	375 (middle)	50 (middle)	4515 (EOL)	0.189	157.02	1.204	33.1	0.60
			1 (BOL)	0.268	235.85	1.136	31.1	1
		
Cell C	500 (high)	30 (low)	500	0.227	236.52	0.959	37.9	0.77
		
			958 (EOL)	0.296	243.34	1.216	43.1	0.60
Cell C	500 (high)	30 (low)	1 (BOL)	0.570	343.92	1.657	30.1	1
		
			200	0.346	316.37	1.094	57.0	0.87
Cell C	500 (high)	30 (low)
			428 (EOL)	0.529	345.95	1.529	63.0	0.60

algorithm. Different combinations of *training and testing* fractions of the total set are considered: 10 %–90 %, 25 %–75 %, 50 %–50 % and 75 %–25 %. We partitioned the dataset in two different ways: randomised and non-randomised partitions. In the first one, the testing dataset was chosen at random from the entire experimental data, from BOL to EOL. In the second one, a training dataset of one portion of the total was selected as the first portion of the data, chronologically from BOL. For instance, in the case of 10 % training/90 % testing, in the not-randomised scenario, the FNN training interval will include the first 451 rows of *cell A* (which has 4515 rows in total), the first 95 rows of *cell B* (which has 958 rows in total) and the first 42 rows for *cell C* (which has

428 rows in total). All the other remaining data, until the End-Of-Life SOH equal to 0.6 will be then used as FNN testing data. The main difference between the randomised and the non-randomised cases is that the latter does not contain a priori knowledge about the information at cell low SOH levels, but only until a certain cell degradation level. The purpose of this scenario is to determine the minimum amount of information from BOL needed to yield accurate results.

In addition to input data, the function itself *feedforwardnet* requires the user to provide a set of parameters that define its architecture and mathematical behaviour. These are the number of FNN hidden layers, the training function algorithm, and several tuning parameters,

Table 3
Combinations of net input data tested.

Combination number	Net input data
1	R_i ; T_{cell} ; P_{cycle} ; SOC_{EOD}
2	R_i ; T_{cell} ; P_{cycle}
3	R_i ; T_{cell} ; SOC_{EOD}
4	R_i ; T_{cell}
5	R_i
6	ΔI ; ΔV
7	T_{cell} ; ΔI ; ΔV
8	T_{cell} ; SOC_{EOD} ; ΔI ; ΔV
9	T_{cell} ; P_{cycle} ; ΔI ; ΔV
10	T_{cell} ; P_{cycle} ; SOC_{EOD} ; ΔI ; ΔV

commonly known as hyperparameters. The training function algorithm was set to Levenberg-Marquardt, the default algorithm used by the function *feedforwardnet* [17]. The number of hidden layers varied between 1 and 10. In this way, for every combination of scenarios and cases tested, 10 different are created, varying the number of hidden layers from 1 to 10. Finally, for every case created, a percentage average estimation error ($\tilde{\epsilon}_{NET}^i$) is defined according to Eq. (3), where i stands for the number of layers tested (it goes from 1 to 10), N_{test} is the total

number of the net testing data (depending on the training-testing percentage rate chosen), $SOH_{estimated}^{ij}$ is the SOH estimated by the net for the j th test data row, which is compared with the real SOH value for the same data row, SOH_{actual}^j .

$$\tilde{\epsilon}_{NET}^i = \frac{100}{N_{test}} \sum_{j=1}^{N_{test}} \left[\frac{|SOH_{estimated}^{ij} - SOH_{actual}^j|}{SOH_{actual}^j} \right] \quad (3)$$

Eq. (3), implemented inside the block “Error definition” of Fig. 4, is then repeated varying the number of hidden layers (i) from 1 to 10 and then the net displaying the minimum $\tilde{\epsilon}_{NET}^i$ is chosen. This lowest $\tilde{\epsilon}_{NET}^i$ is called $\tilde{\epsilon}_{NET}$ (final output of the process of Fig. 4) and will be the benchmark against which the parameters all the tested combination of scenarios and cases will be compared.

3.1.1. Randomised dataset results

This section shows the estimation errors in the FNN trained with the dataset which is first subjected to a randomisation process, through the default MATLAB function *randperm*. Figs. 5 and 6 show how the SOH estimation results appear, for two specific combinations of all the analysed cases. Specifically, the cases graphically reported in Figs. 5 and 6 share the same training-testing ratio (50 %–50 %) but they are

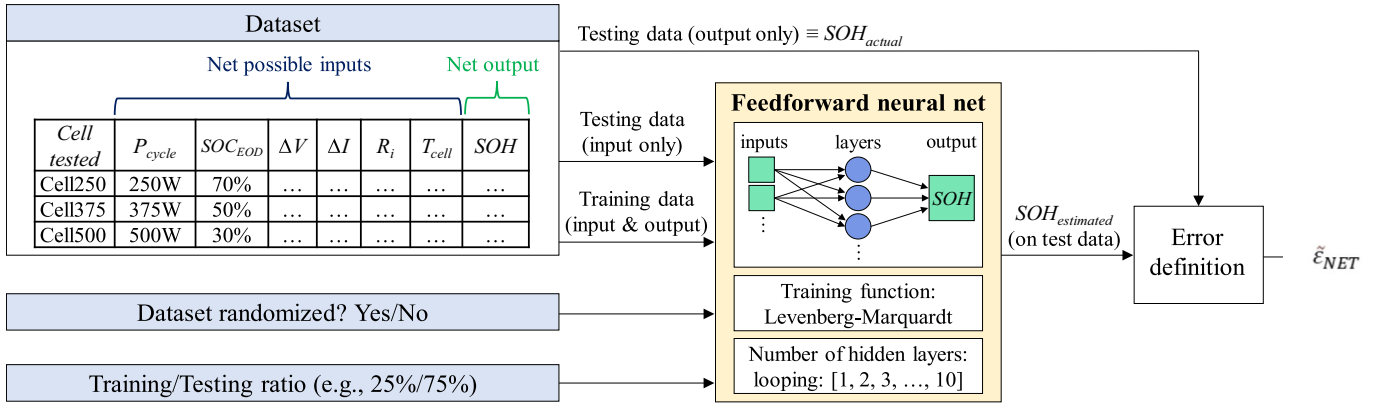


Fig. 4. Schematisation of the FNN design and testing procedure.

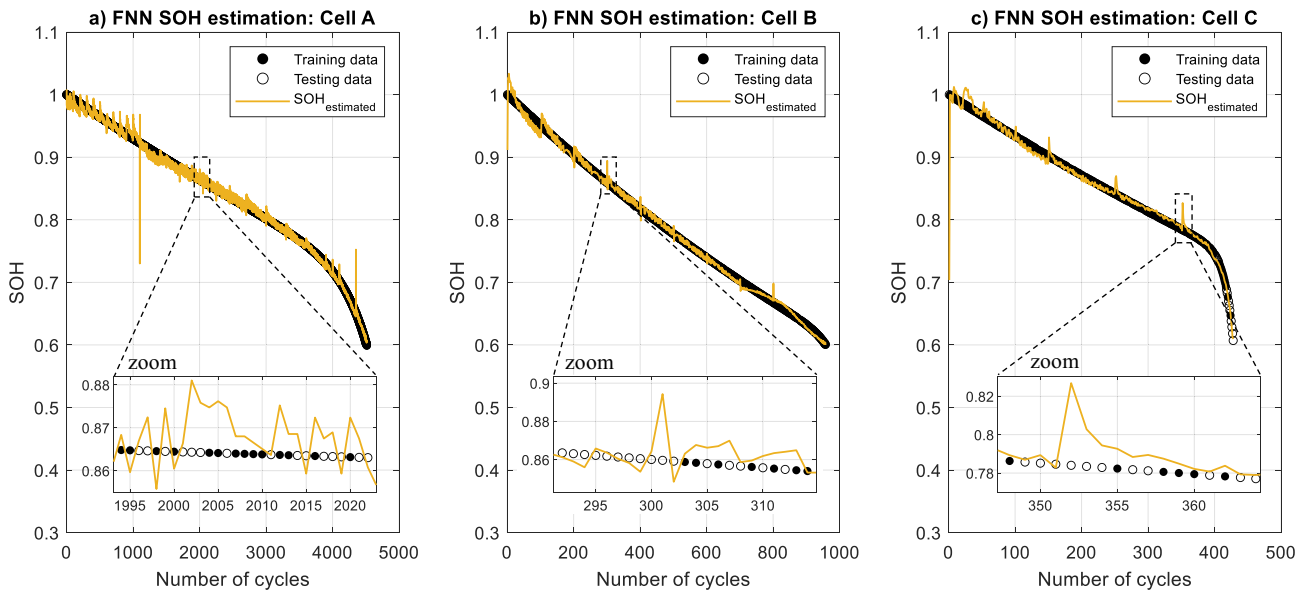


Fig. 5. FNN SOH estimation for the scenario of randomised dataset giving as net input information the combination 10 of Table 3: T_{cell} ; P_{cycle} ; SOC_{EOD} ; ΔI ; ΔV . Case training-testing ratio = 50 %–50 %. Filled circles: training data, empty circles: testing data (appreciable in the zoom sub-plots). Plot a): Cell A results, plot b): Cell B results, plot c): Cell C results.

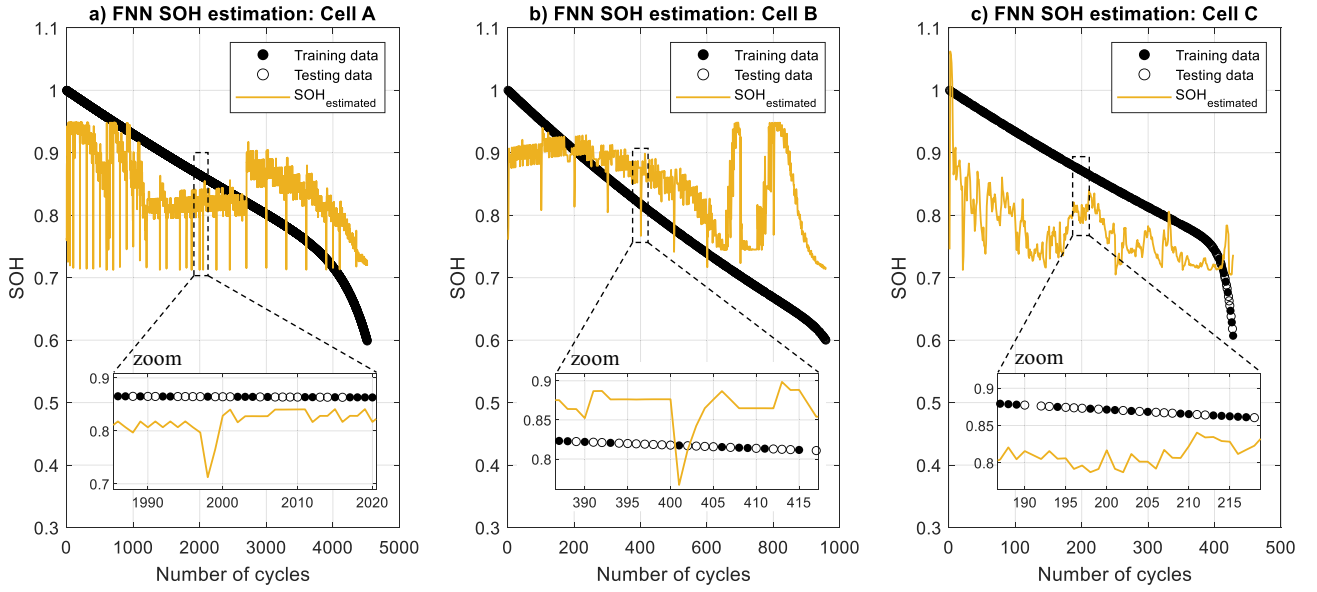


Fig. 6. FNN SOH estimation for the scenario of randomised dataset giving as net input information the combination 5 of Table 3: R_i . Case training-testing ratio = 50 %–50 %. Filled circles: training data, empty circles: testing data (appreciable in the zoom sub-plots). Plot a): Cell A results, plot b): Cell B results, plot c) Cell C results.

representative of two different input conditions: Fig. 5 displays the results of the FNN which is given, as input data, the combination with the maximum number of information available (combination number 10 in Table 3, e.g. T_{cell} , P_{cycle} , SOC_{EOD} , ΔI , ΔV). Fig. 6, instead, displays the results of the FNN which is given the combination with the minimum amount of input data (combination number 5 in Table 3, e.g., R_i). In both the figures, the training and testing data (taken from the dataset of Table 2) for the SOH value are respectively reported in black filled circles and empty circles, while the net output SOH estimation ($SOH_{estimated}$) is depicted as a yellow line. Regarding the $SOH_{estimated}$ plotted in these figures (Figs. 5 and 6), it is here important to state that although (for results visualisation purposes) the $SOH_{estimated}$ is evaluated and plotted not only over testing data but also over training data, the evaluation of the net output estimation SOH error ($\tilde{\epsilon}_{NET}$), is calculated on testing data only, as said accordingly to (3).

The results of Figs. 5 and 6 show the SOH estimation as a function of

the cycle power level. Irrespective of the choice of input, or randomisation scenario, estimation errors $\tilde{\epsilon}_{NET}$ always show consistent behaviour. The accuracy is not dependent of the cycle power level. All the obtained final SOH estimation errors are then reported in Fig. 7 for all the tested cases. Moreover, observing Fig. 5, Cell C, some spikes in the $SOH_{estimated}$ curve are visible, which represent the higher errors achieved by the net. If we now take as reference Fig. 3, Cell C, it is possible to correlate the spikes behaviour of Fig. 5, Cell C, with the relative temperature T_{cell} given as input. Indeed, all the single spikes are related to the input data points that show different temperatures among the average trend (blue dots of Fig. 3) which, after the randomisation process, are not chosen as training data. As visible example, the spike observed in the zoom plot of Fig. 5, Cell C, is achieved in correspondence of around cycle number 350, where a series of testing data appear (empty circles), and, as visible in Fig. 3, a “cold” point is registered.

Fig. 7 shows the apparent independence of the predictive accuracy of

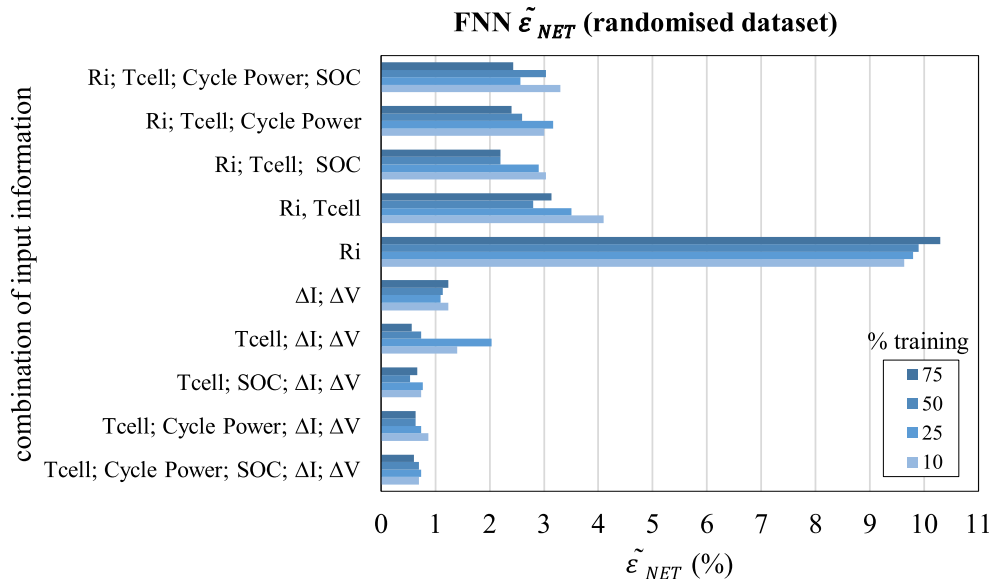


Fig. 7. FNN average percentage error on testing data, for the randomised scenario, as a function of the different combination of input information and of the training-testing ratio.

training-test ratio variation.

Cases that include R_i as the sole input data show the highest errors. If the R_i information is omitted and ΔV and ΔI are provided, the error decreases considerably. This observation reveals that ΔV and ΔI are essential inputs if an error in the order of 1 % is desired. This is an interesting observation since the internal resistance R_i is calculated directly from ΔV and ΔI , indicating that the neural network is unable to perform this feature extraction by itself under the present training conditions. In addition, additional inputs (such as T_{cell} , SOC_{EOD} , P_{cycle}) also decrease the overall error $\tilde{\epsilon}_{NET}$. The best case is reached for input combination number 8 and training-testing ratio 50 %–50 %, with $\tilde{\epsilon}_{NET} = 0.5$ %.

3.1.2. Non-randomised dataset results

This section shows the results achieved by training the FNN with aging data given chronologically until the value of the training percentage defined is reached. The FNNs created in this way are trained with data up to a certain level of SOH and they are tested to predict the subsequent SOH trend. For example, a training-testing ratio of 25 %–75 % means that the neural net is trained with the first 25 % of the data and is tested on the remaining 75 %. Figs. 8 and 9 display the results obtained for the not randomised scenario, respectively giving as net input information the combination 10 and 5 of Table 3, both having a training-testing ratio = 50 %–50 %. Black circles indicate training data and blue circles indicate testing data. The FNN output ($SOH_{estimated}$) is still evaluated for the entire dataset while the SOH estimation error $\tilde{\epsilon}_{NET}$, as reported for all cases in Fig. 10, is calculated on the testing data only.

Error results displayed in Fig. 10, show that SOH estimation errors using a not randomised dataset are sensitive to the training-testing percentage chosen: as expected, the larger the amount of training data, the higher the accuracy.

The overall accuracy of the non-randomised scenario was lower than that of the randomised scenario, showing the lowest errors in the cases that included ΔV and ΔI , and selecting a percentage of training equal to or higher than 50 %. The best case corresponds to input combination number 9 and a training-testing ratio = 50 %–50 %, resulting in $\tilde{\epsilon}_{NET}$ equal to 2.4 %.

3.2. Comparison with other methods

Over the past few years, many techniques have been developed to estimate the state of charge and the state of health of lithium-ion cells.

- Electro-chemical model methods. This method is strongly theoretical and tries to emulate models the elaborate internal electrochemical reactions of the battery. These models are complex and require large computing resources. These models are not able to correctly predict under dynamic real-life conditions, and hence are not preferred for real-time estimation [18].
- Equivalent circuit model methods. The equivalent circuit model among the most popular methods used to determine the SOH. It relies on a building an electrical model to depict the lithium-ion battery, generally using multiple R-C pairs. The accuracy of the model increases by increasing the number of R-C pairs, but so does the complexity of the model, slowing down its response under dynamic conditions. The Kalman Filter and its nonlinear versions (EKF, UKF) typically use an equivalent circuit to perform its estimation and correction steps.
- Statistical methods, as in [19]. This category encompasses Machine Learning (e.g., Gaussian Process Regression, Support Vector Machines, decision trees, etc.) and Deep Learning methods (e.g., feed-forward (FNN) and recurrent (CNN, LSTM) neural networks). They work by training a function with a large amount of experimental data that includes inputs (called predictors) and outputs (called responses). Typically, Machine Learning methods require the user to define a set of features from the data and aims at identifying pattern of change in those features. Deep Learning methods, on the other hand, use more training data but do not require the user to extract features from the data since they can extract those features automatically.

The FNN, a relatively simple type of neural network implemented in this work, rapidly and accurately converges to the estimated SOC and SOH under dynamic conditions and does not depend upon initial conditions. A comparison of the different methods in terms of estimation errors over different methodologies and batteries adopted is summarised in Table 4 below, which shows that the proposed FNN method yields

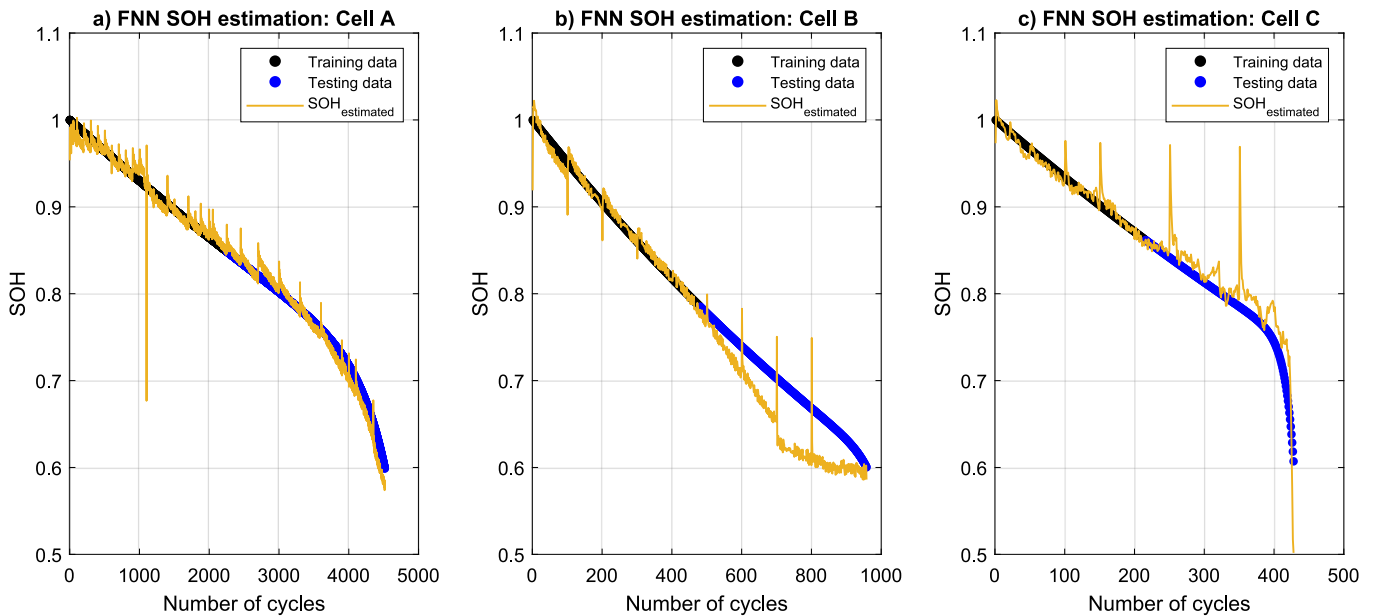


Fig. 8. FNN SOH estimation for the scenario of not-randomised dataset giving as net input information the combination 10 of Table 3: T_{cell} ; P_{cycle} ; SOC_{EOD} ; ΔI ; ΔV . Case training/testing ratio = 50 %/50 %. Black circles: training data, blue circles: testing data. Plot a): Cell A results, plot b): Cell B results, plot c): Cell C results. (For interpretation of the references to color in this figure legend, the reader is referred to the web version of this article.)

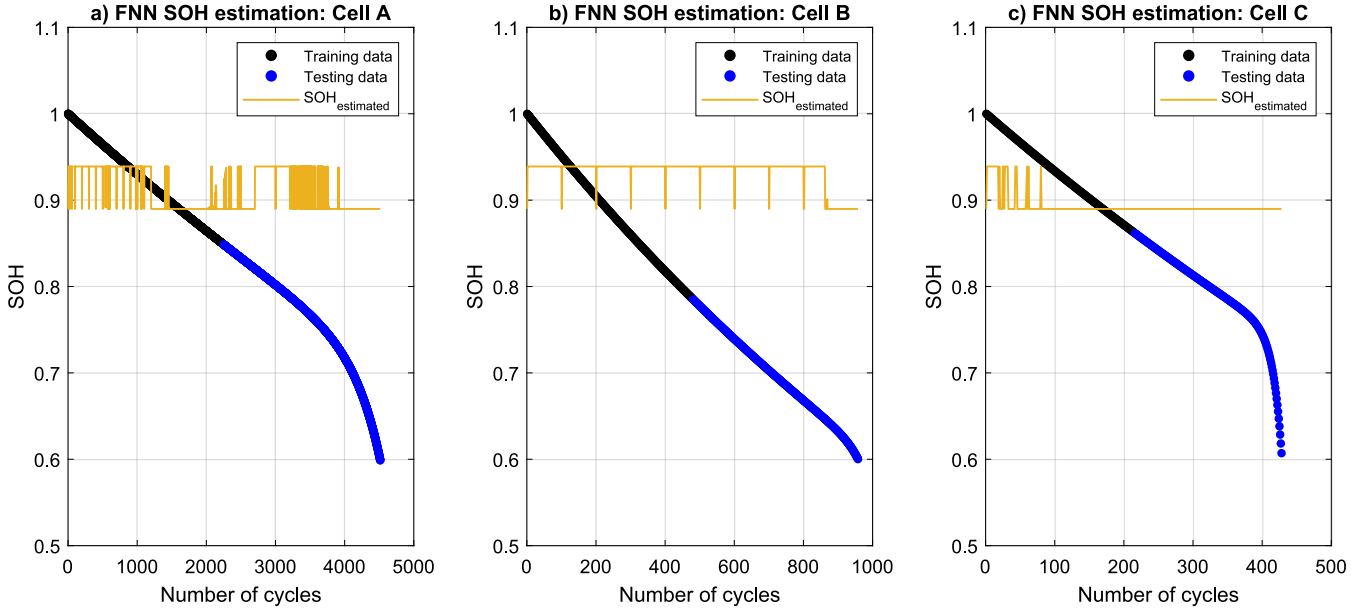


Fig. 9. FNN SOH estimation for the scenario of not-randomised dataset giving as net input information the combination 5 of Table 3: Ri. Case training/testing ratio = 50 %/50 %. Black circles: training data, blue circles: testing data. Plot a): Cell A results, plot b): Cell B results, plot c) Cell C results. (For interpretation of the references to color in this figure legend, the reader is referred to the web version of this article.)

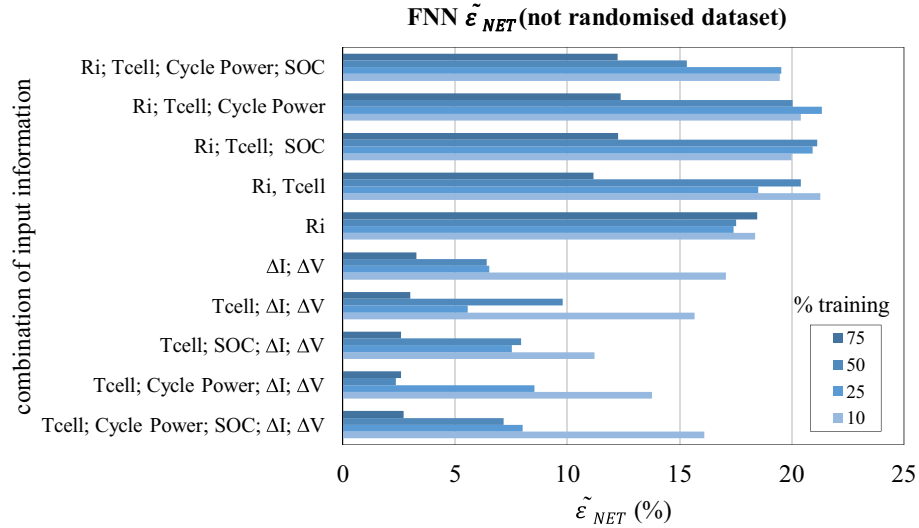


Fig. 10. FNN average percentage error on testing data, for not randomised scenario, in function of the different combination of input information given to the net and in function of the training/testing ratio.

results comparable to those reported in the literature.

As a means of comparison against other methods, we trained a Gaussian Process Regression model. This function is part of MATLAB's Statistics and Machine Learning Toolbox, and accessible through the Regression Learner App. We reproduced the conditions shown in Table 3 with a testing/training ratio equal to 75 %/25 %. The results of this approach (labelled "RL") are shown in the second row of Table 4, demonstrating a comparable degree of accuracy if compared to the FNN achievement (0.4 % mean absolute error vs 0.5 %).

4. Application of the proposed approaches to estimate the SOH of a calendar aged cell

Based on the results described in Sections 3.1 and 3.2, after the selection of the best case of input information to be given as SOH predictors, the FNN and the RL approaches here presented have shown

similar behaviour, with acceptable values of mean absolute error (MAE). However, this error values result of a validation procedure applied to the same lithium cells used for the training process of the AI-based functions adopted (FNN and RL). It is therefore interesting to evaluate if the same FNN and RL functions trained as described in paragraph 3.1 and 3.2, with the dataset coming from the three lithium cells described in chapter 2, can be used to estimate the SOH of a cell of the same kind but with a complete different aging history. To this end, a 60 Ah LFP cell, nominally identical to the three ones used in chapter 2 but degraded only by calendar aging for at least 3 years without ever being cycled is used.

In the first place, the SOH level of this last cell has been determined by a full charge/discharge test, as described in chapter 2, with a resulting extracted capacity equal to 68 Ah. According to the definition of Eq. (1), and knowing the beginning of life capacity value of this cell measured at the very same test conditions ($C_{BOL} = 72$ Ah), the actual calculated SOH is equal to 0.94. Secondly, the cell, previously fully

Table 4

Comparison between different State-of-Health estimation methods: errors are expressed as Mean Absolute Error (MAE) or Root Mean Square Error (RMSE).

SOH estimation method	Lowest error achieved	Battery	Temperature range
FNN	0.5 % (MAE)	LFP 60 Ah	20 ÷ 65 °C
RL (GPR-based)	0.4 % (MAE)	LFP 60 Ah	20 ÷ 65 °C
FNN [20]	0.7 % (RMSE)	Li-ion (not specified) 3 Ah	0 ÷ 60 °C
FNN [21]	0.8 % (MAE)	LFP 2 Ah	25 °C
FNN [22]	2 % (MAE)	LFP 2 Ah	25 °C
RL (GPR-based) [23]	0.3 % (MAE)	NMC 21 Ah	35 ÷ 45 °C
RNN [24]	0.5 % (RMSE)	NMC 100 Ah	40 ÷ 50 °C
RNN [25]	0.4 % (MAE)	Li-ion (not specified) 2 Ah	4 and 24 °C
LSTM [22]	1 % (MAE)	LFP 2 Ah	25 °C
LSTM [25]	1.8 % (MAE)	Li-ion (not specified) 2 Ah	4 ÷ 24 °C
LSTM [26]	0.5 % (MAE)	Li-ion (not specified) 2 Ah	4 ÷ 43 °C
EKF [27]	0.6 % (MAE)	Li-ion (not specified)	Not specified
EKF [28]	1.4 % (MAE)	NMC 2 Ah	0 ÷ 45 °C

charged, has been completely discharged applying a specific experimental cycle, shown in Fig. 11 replicating the power profiles used in chapter 2 for the training procedure of the FNN and the RL.

Specifically, the test consisted of the repetition of constant power discharge and charge steps, followed by a pause. These three phases (discharge-charge-pause) have the same duration of 30 s. The same pattern is therefore repeated cyclically increasing the constant power level, according to the three levels already used for the FNN and RL training dataset (250, 375 and 500 W). The consequence of the application of such a power profile to the cell under study is a slow decreasing of the cell SOC, as can be seen from Fig. 11, which shows the SOC window from 68 to 62 % for clarity. The cell is placed in a climatic chamber with a temperature set-point of 25 °C, while the cell surface temperature reaches a stabilized thermal regime of around 35.5 °C.

As done in chapter 2 in order to achieve the information for the dataset in Table 2, every time the cycle profile moves from the end of a discharging step to the beginning of a charging step, a set of predictors is

calculated. Based on the results described in paragraph 3.1 and 3.2, we choose combination 8 of Table 3, selecting the predictors T_{cell} , SOC_{EOD} , ΔI and ΔV as information data to be given as input to both the FNN and RL here proposed, as illustrated in Fig. 12.

While the testing conditions of the cycling aging study only allowed the calculation of the predictors at three SOC levels (70 %, 50 %, and 30 % for the 250 W, 375 W, and 500 W, respectively), it is now possible to make the estimation at any SOC level since the pulsed discharge used here drives the battery SOC continuously down from full charge. Fig. 13 displays the results of this last test, showing the SOH estimations as a function of SOC for the two approaches, compared with the actual SOH of the cell under test (0.94). The FNN results are shown in Fig. 13a) and the RL results are visible in Fig. 13b). We specify that the FNN and the RL chosen have been trained with the same randomised scenario with 75 %/25 % testing/training ratio and with the same set of predictors, which is the combination number 8 of Table 3. In addition, the color legend of Fig. 13 indicates the divisions among the three level of power each single SOH estimation derive: respectively blue, cyan and yellow for 250, 375 and 500 W power steps.

Observing the results of Fig. 13, it is possible to draw the following conclusions.

- The estimation from the FNN only gave a reasonable result at SOC levels close to the three SOC levels at which the net had been trained ("high" SOC around 70 %, "middle" SOC around 50 % and "low" SOC around 30 %), with unsatisfactory results when applied at other SOC levels.
- The RL approach -Fig. 13b)- shows a more robust behaviour when applied to the calendar aged cell. As shown in Fig. 13b), the cell SOH is closely matched by the $SOH_{estimated}^{RL}$ specifically for the conditions of power step of 250 W. For this case, the actual SOH is estimated with a mean absolute error (MAE) of 4.5 % over the whole SOC window (from 90 to 20 %).

5. Conclusions

Using battery cycling data at different power levels, this paper shows that AI methods can estimate the State-of-Health of an LFP battery to a degree of accuracy acceptable for commercial applications. A

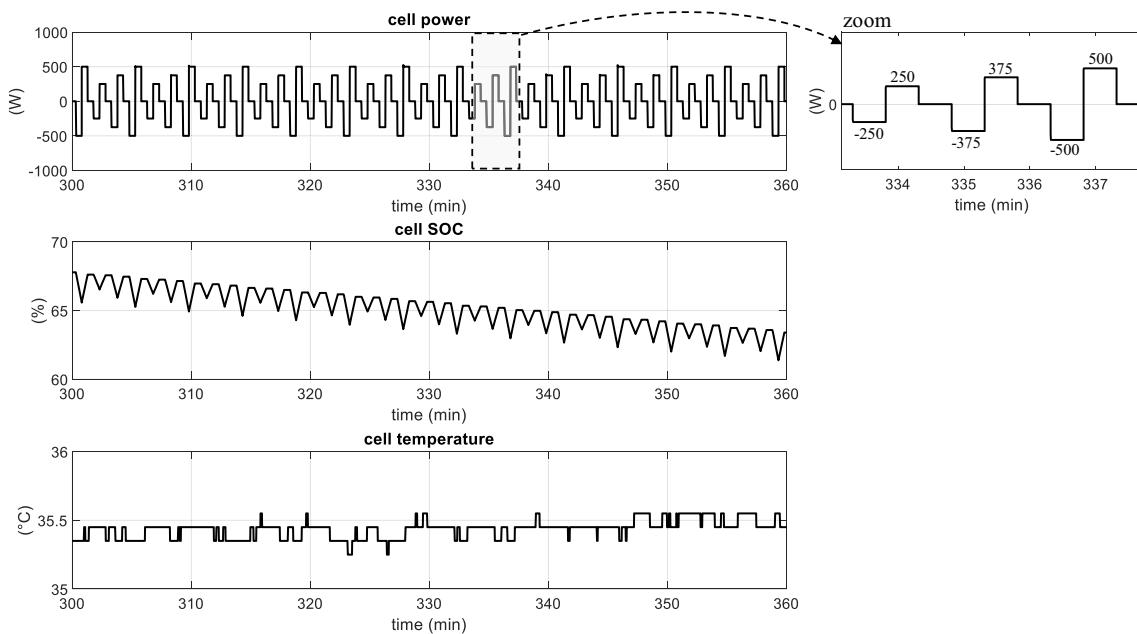


Fig. 11. Experimental test performed on the cell aged by calendar: cell power, SOC and temperature; zoom of the power profile pattern continuously repeated until the cell is fully discharge. For graphical representation reason, only the 5th hour of the test is shown, for a SOC window moving from 68 to around 62 %.

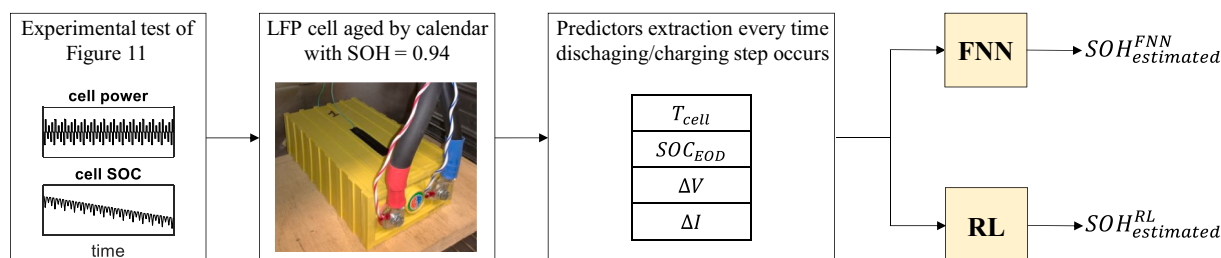


Fig. 12. Schematisation of the procedure for the application of the FNN and the RL approaches to estimate the SOH of the cell aged by calendar.

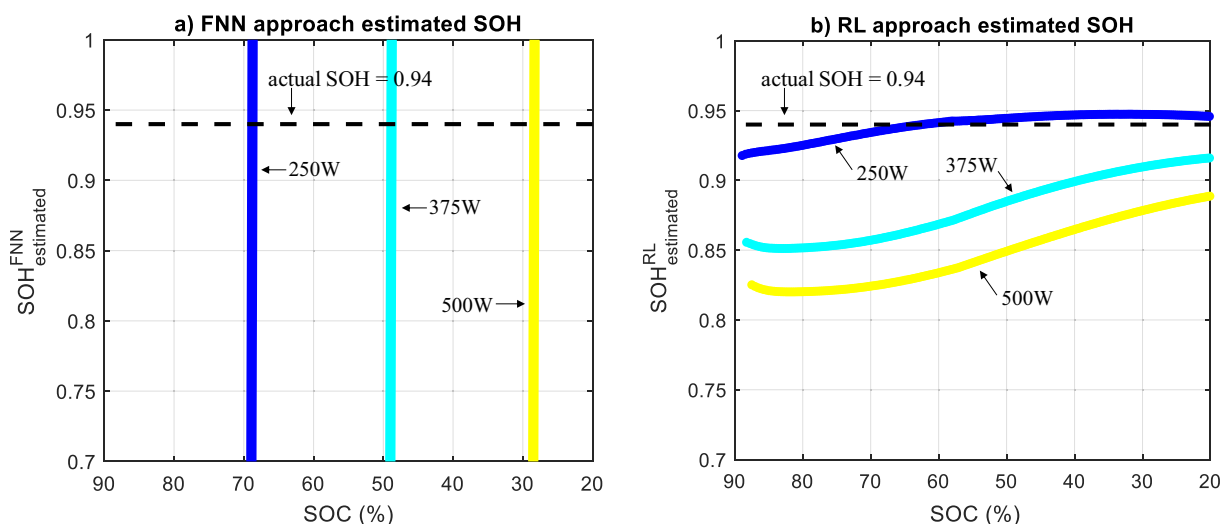


Fig. 13. Results of the application of the FNN and RL approaches to the LFP cell aged by calendar: a) SOH estimated by the FNN displayed in function of the cell SOC; b) SOH estimated by the RL displayed in function of the cell SOC. Color legend means the division among the three level of power each SOH estimation derives: blue = 250 W, cyan = 375 W and yellow = 500 W. Dashed black lines represent the cell under test actual SOH value. (For interpretation of the references to color in this figure legend, the reader is referred to the web version of this article.)

Feedforward Neural Network is developed and trained with battery on-line field data, like cell voltage, current, temperature and State-of-Charge, which are always available in every battery application.

Results showed that training the neural network with a randomised dataset taken from the entire battery lifetime yielded the best results, with State-of-Health estimation average errors lower than 1 %. However, if the same FNN is trained with non-randomised dataset, but only with partial information, chronologically starting from the Beginning-Of-Life of the battery, it is still possible to correctly estimate the battery remaining life SOH trend with average errors in the range of 0 to 5 %, provided that the battery SOC is greater than 50 %.

Secondly, we observed that using voltage and current as inputs resulted in a lower estimation error than using internal resistance, even though internal resistance is calculated as the ratio of voltage to current, showing that it is convenient to perform feature extraction. Moreover, best case results are reached only if the battery temperature is included as FNN input information.

Finally, the FNN method is compared to a Gaussian Process Regression (GPR) and tested on a cell that had been calendar aged. The FNN estimation accuracy on a cell with calendar aging was only acceptable when the battery cell was at the SOC levels corresponding to those at which the FNN had been trained. Conversely, the GPR prediction on calendar aged cells showed acceptable error levels.

Declaration of competing interest

The authors declare that they have no known competing financial interests or personal relationships that could have appeared to influence the work reported in this paper.

Data availability

Data will be made available on request.

References

- [1] A.K. Padhi, K.S. Nanjundaswamy, J.B. Goodenough, Phospho-olivines as positive-electrode materials for rechargeable lithium batteries, *J. Electrochem. Soc.* 144 (1997) 1188–1194.
- [2] V.B. Ratnakumar, C.S. Marshall, Lithium plating behavior in lithium-ion cells, *Electrochemical Society, Inc, ECS Transactions* 25 (2010) 241–252.
- [3] K.G. Gallagher, S.E. Trask, C. Bauer, et al., Optimizing areal capacities through understanding the limitations of lithium-ion electrodes, *Journal of The Electrochemical Society* 163 (2015), A138.
- [4] P. Arora, M. Doyle, R.E. White, Mathematical modeling of the lithium deposition overcharge reaction in lithium-ion batteries using carbon-based negative electrodes, *Journal of The Electrochemical Society* 145 (1999) 3543–3553. The Electrochemical Society.
- [5] D. Anseán, M. Dubarry, A. Devie, et al., Operando lithium plating quantification and early detection of a commercial LiFePO₄ cell cycled under dynamic driving schedule, *Journal of Power Sources* 356 (2017) 36–46. Elsevier.
- [6] P. Prezas, L. Somerville, P. Jennings, et al., Effect of fast charging of lithium-ion cells: performance and post-test results, in: *SAE Technical Paper 2016-01-1194*, SAE, 2016.
- [7] R. Chandrasekaran, Quantification of bottlenecks to fast charging of lithium-ion-insertion cells for electric vehicles, *Journal of Power Sources* 271 (2014) 622–632. Elsevier.
- [8] D. Anseán, M. González, J. Viera, et al., Fast charging technique for high power lithium iron phosphate batteries: a cycle life analysis, *J. Power Sources* 239 (2013) 9–15.
- [9] M. Dubarry, C. Truchot, B.Y. Liaw, Synthesize battery degradation modes via a diagnostic and prognostic model, *Journal of power sources* 219 (2012) 204–216. Elsevier.
- [10] P. Arora, R.E. White, M. Doyle, Capacity fade mechanisms and side reactions in lithium-ion batteries, *Journal of The Electrochemical Society* 145 (1998) 3647–3667. The Electrochemical Society, October.

- [11] J. Vetter, P. Novák, M.R. Wagner, et al., Ageing mechanisms in lithium-ion batteries, *Journal of Power Sources* 147 (2005) 269–281. Elsevier.
- [12] M. Broussely, S. Herreyre, P. Biensan, et al., Aging mechanism in Li ion cells and calendar life predictions, *Journal of Power Sources* 97–98 (2001) 13–21. Elsevier B. V.
- [13] M. Ceraolo, G. Lutzemberger, D. Poli, C. Scarpelli, Experimental evaluation of aging indicators for lithium–iron–phosphate cells, *Energies* 14 (2021) 4813, <https://doi.org/10.3390/en14164813>.
- [14] Matlab-Simulink official site, <https://www.mathworks.com/products/simulink.html>.
- [15] A. Barai, K. Uddin, W.D. Widanage, et al., Study of the influence of measurement timescale on internal resistance characterisation methodologies for lithium-ion cells, *Sci. Rep.* 8 (2018) 21.
- [16] Feedforward net library official site, <https://www.mathworks.com/help/deeplearning/ref/feedforwardnet.html>.
- [17] H. Yu, B.M. Wilamowski, Levenberg-Marquadt Training, Intelligent Systems, CRC Press, 2011.
- [18] E. Locorotondo, V. Cultrera, L. Pugi, L. Berzi, M. Pierini, G. Lutzemberger, Development of a battery real-time state of health diagnosis based on fast impedance measurements, *J. Energy Storage* 38 (2021), 102566.
- [19] G.C.S. Almeida, A.C.Z.D. Souza, P.F. Ribeiro, A neural network application for a lithium-ion battery pack state-of-charge estimator with enhanced accuracy, *Proceedings* 58 (2020) 33.
- [20] G.-W. You, S. Park, D. Oh, Real-time state-of-health estimation for electric vehicle batteries: a data-driven approach, *Appl. Energy* 176 (Aug. 2016) 92–103.
- [21] J. Wu, Y. Wang, X. Zhang, Z. Chen, A novel state of health estimation method of li-ion battery using group method of data handling, *J. Power Sour.* 327 (Sep. 2016), 457464.
- [22] Z. Xia, J.A. Abu Qahouq, Adaptive and fast state of health estimation method for lithium-ion batteries using online complex impedance and artificial neural network, in: 2019 IEEE Applied Power Electronics Conference and Exposition (APEC), 2019, pp. 3361–3365.
- [23] K. Liu, X. Hu, Z. Wei, Y. Li, Y. Jiang, Modified gaussian process regression models for cyclic capacity prediction of lithium-ion batteries, *IEEE Trans. Transport. Electr.* 5 (4) (Dec. 2019) 1225–1236.
- [24] A. Eddahech, O. Briat, N. Bertrand, J.-Y. Delétage, J.-M. Vinassa, Behavior and state-of-health monitoring of Li-ion batteries using impedance spectroscopy and recurrent neural networks, *Int. J. Electr. Power Energy Syst.* 42 (1) (Nov. 2012) 487–494.
- [25] M. Raman, V. Champa, V. Prema, State of health estimation of lithium ion batteries using recurrent neural network and its variants, in: 2021 IEEE International Conference on Electronics, Computing and Communication Technologies (CONECCT), 2021, pp. 1–6.
- [26] G. Crocioni, D. Pau, J.-M. Delorme, G. Gruosso, Li-ion batteries parameter estimation with tiny neural networks embedded on intelligent IoT microcontrollers, *IEEE Access* 8 (2020) 122135–122146.
- [27] Zengyuan Bian, Yan Ma, An improved particle filter method to estimate state of health of lithium-ion battery, *IFAC-PapersOnLine* 54 (10) (2021) 344–349.
- [28] C.-Q. Du, J.-B. Shao, D.-M. Wu, Z. Ren, Z.-Y. Wu, W.-Q. Ren, Research on co-estimation algorithm of SOC and SOH for lithium-ion batteries in electric vehicles, *Electronics* 11 (2022) 181.